Versatile Biogenic Electrolytes for Highly Performing and Self-Stable Light-Emitting Electrochemical Cells

Luca M. Cavinato, Gonzalo Millán, Julio Fernández-Cestau, Elisa Fresta, Elena Lalinde, Jesús R. Berenguer,* and Rubén D. Costa*

Light-emitting electrochemical cells (LECs) are the simplest and cheapest solid-state lighting technology for soft and/or single-use purposes. However, a major concern is a transition toward eco-friendly devices (emitters/electrolytes/electrodes) to meet green optoelectronic requirements without jeopardizing device performance. In this context, this study shows the first biogenic electrolyte applied to LECs, realizing self-stable and highly performing devices with cellulose-based electrolytes combined with archetypical emitters (conjugated polymers or CPs and ionic transition-metal complexes or iTMCs). In contrast to reference devices with traditional electrolytes, self-stability tests (ambient storage/thermal-stress) show that devices with this bio-electrolyte hold film roughness and photoluminescence quantum yields over time. In addition, charge injection is enhanced due to the high dielectric constant, leading to high efficacies of 15 cd A^{-1}@3750 cd m^{-2} and 2.5 cd A^{-1}@600 cd m^{-2} associated with stabilities of 3000/7.5 h and 153/0.7 J for CPs/iTMCs-LECs, respectively. They represent four-/twofold enhancement compared to reference devices. Hence, this novel biogenic electrolyte approach does not reduce device performance as in the prior-art bio-degradable polymer and DNA-hybrid electrolytes, while the easiness of chemical modification provides plenty of room for future developments. All-in-all, this study reinforces the relevance of carbohydrate-based electrolytes not only for energy-related applications, but also for a new field in lighting.

1. Introduction

In the past decades, three technologies have emerged as simple and low-cost solid-state lighting devices: polymeric light-emitting diodes (PLEDs), light-emitting electrochemical cells (LECs), and, recently, perovskite light-emitting diodes (PeLED). While the former are purely electronic devices, LECs and PeLEDs show mixed ionic-electronic nature.[1] The rearrangement of mobile ions close to the electrode interfaces in response to an applied external bias leads to the formation of electrical double layers (EDLs), facilitating efficient charge injection at low applied bias.[2,3] Subsequently, the growth of p- and n-doped regions at the electrode frontiers is also controlled by the presence of ions, while the inner zone remains neutral (intrinsic region or i) as exciton formation and relaxation occur. Thus, a dynamic p-*i*-n junction is formed in the active layer, which sustains charge injection, transport, and exciton formation processes using a single electroactive layer.[3] Here, the electrolyte is key as it allows the formation of EDLs and stabilizes the p-*i*-n junction over time.[4,5] This results in the use of air-stable electrodes and a fairly tolerance to the active layer thickness that are the greatest technological advantages over PLEDs.[6] In addition, low fabrication cost and moderate device performance make LECs interesting for soft lighting applications (decoration, labeling, phototherapy, *etc.*) and disposable electronics (biodegradable and recyclable devices) that are of high interest due to their low environmental footprint. Thus, the transition toward eco-friendly LECs is becoming urgent to set in its market niche in the short term.[7]

In this context, huge efforts have been carried out to introduce ecological emitters in LECs (iTMCs,[8,9] small molecules,[10,11] carbon dots,[12] etc.), while little consideration has been placed on green ionic electrolytes. On one hand, a few examples of eco-friendly polymer-electrolytes have been reported: i) biodegradable electrolytes based on poly(lactic-co-glycolic acid), poly(ε-caprolactone), and poly(ε-caprolactone-co-trimethylene carbonate) with CPs achieving moderate performances (*i.e.*, 30 h and efficacy of 3.2 cd A^{-1}@262 cd m^{-2}),[13–15] and ii) bio-hybrid electrolytes

L. M. Cavinato, J. Fernández-Cestau, E. Fresta, R. D. Costa
Chair of Biogenic Functional Materials
Technical University of Munich
Schulgasse 22, D-94315 Straubing, Germany
E-mail: ruben.costa@tum.de
G. Millán, E. Lalinde, J. R. Berenguer
Departamento de Química-Centro de Investigación en Síntesis Química (CISQ)
Universidad de La Rioja
Madre de Dios 53, Logroño E-26006, Spain
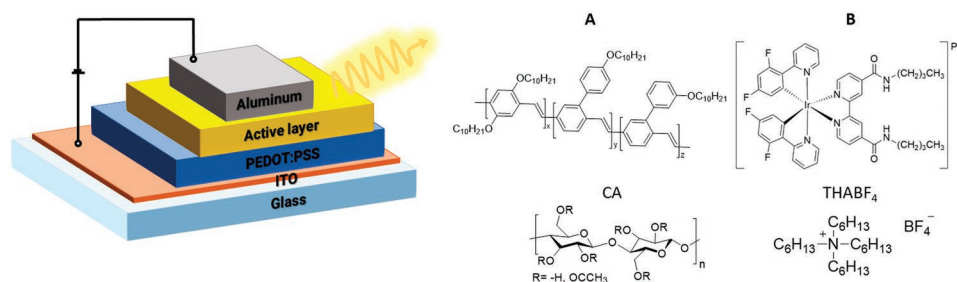E-mail: jesus.berenguer@unirioja.es

Figure 1. Left, Sketch of a LEC. Right, Chemical structures of the active layer constituents.

(DNA-cetyltrimethylammonium) with CPs (1 h and efficacy of 1 cd A^{-1}@1650 cd m^{-2}).[16] Unfortunately, all these devices came with a trade-off with respect of the device performance (see Table S1, Supporting Information).[14,16–18] On the other hand, self-stability with respect to ambient storage and mechanical/thermal stress has been barely explored. Here, we have pinpointed superior self-stable LECs using ionic polyelectrolytes and Ir-iTMCs compared with those with traditional ionic liquids.[18]

Herein, we demonstrate a third family of green electrolytes leading to highly self-stable and performing LECs that outperform their respective traditional LECs references. This consists of a fully biogenic cellulose-based electrolyte that is, in addition, highly versatile with respect to the type of emitters, namely Super yellow as CP (**A**) and [Ir(dfppy)$_2$(dbbpy)]PF$_6$ (dfppy is 2-(2,4)-difluorophenyl-pyridinyl and dbbpy is *N,N′*-dibutyl-2,2′-bipyridine-4,4′-dicarboxamide) as Ir-iTMCs (**B**) (**Figure 1**). In particular, cellulose acetate (CA) was selected as an ion transporter due to its abundance and low-cost, high ionic conductivity, wide electrochemical stability window, high solubility in organic solvents, and good mechanical properties.[19–21] As ions source tetrahexylammonium tetrafluoroborate (THABF$_4$) was selected, due to its wide electrochemical stability window.[22] We rationalize the optimization of the active layers (CA:THABF$_4$:CP or Ir-iTMC) with respect to their morphological, photoluminescence, self-stability, and ion conductivity features. This resulted in devices with superior performances (stability/efficacy/brightness) compared to their respective references (embedding 0 wt%. of CA) for each type of emitter. In short, the best CA-based LECs with CP/Ir-iTMC emitters featured luminances of 3750/600 cd m^{-2}, efficacies of 15/2.5 cd A^{-1}, and stabilities of 153/0.7 J, resulting in four-/twofold enhancement with respect to that of the references. In contrast to prior-art in ecological polymer electrolytes for LECs, a green transaction is, therefore, possible without jeopardizing device performance and self-stability using fully biogenic electrolytes. What is more, this work is a landmark in the integration of polysaccharide-based electrolytes in lighting devices, as traditionally they have been exclusively implemented as substrates.[23] Hence, our findings strongly reinforce the relevance of carbohydrate-based materials/components towards the green transition in (opto)electronics focused not only for energy-related[24,25] and photonics[26] applications, but also now for lighting purposes beyond the traditional application of cellulose-based substrates.

2. Results and Discussion

2.1. Notes about Fabrication and Composition of CA-based Films

The influence of the blend composition (i.e., mass ration between **A** or **B** emitters, CA, and THABF$_4$) on the morphology, photoluminescence, self-stability, and ion conductivity of thin-films (80-100 nm) prepared via spin-coating technique from solutions with the desired ratio was our first focus. Based on the changes in the above figures (vide infra), CA mass ratio ranged from 0% (reference) to 30% *wt.*, while the optimum THABF$_4$ concentration was calculated following Equation 1:[27,28]

$$z = \frac{m_{salt}}{m_{emitter}} = \frac{\chi_{doping}\left(d_{tot} - d_{pn}\right)M_{salt}}{2d_{tot}M_{emitter}} \qquad (1)$$

where z is the mass ratio between salt and emitter, m_{salt} is the mass of the former, $m_{emitter}$ is the mass of either **A** or **B**, χ_{doping} is the desired doping concentration (i.e., 1.2 to compensate for side-reactions), d_{tot} is the active layer thickness, d_{pn} is the thickness of the undoped region (i.e., assumed 20 nm), M_{salt} is the molar mass of ion source, and $M_{emitter}$ is the molar mass of the emitter. Consequently, we used 20 wt.% THABF$_4$ in all the configurations.

Topography and viscoelastic mapping of the thin-films were studied using Atomic Force Microscopy (AFM). While films blending **A** and CA show an excellent morphology (vide infra), those with the benchmark [Ir(ppy)$_2$(dtbbpy)]PF$_6$, namely bis[phenylpyridinyl][(4,4′-tertbutyl)-2,2′-bipyridine-N1,N1′] Iridium(III) hexafluorophosphate,[29] led to segregation between the two components with evident aggregates (Figure S1, Supporting Information). Phase separation features and undesired pin-hole structures upon either fabrication or storage/thermal stress dramatically affect the p-*i*-n formation/stabilization and, in turn, the device performance.[30,31] Thus, the compatibility between Ir-iTMCs and CA was nicely enhanced by substituting the *tert*-butyl moieties with a short alkyl chain bonded trough amidic bond in complex **B** (Figure 1). This was synthetized following reported methods and it has thoughtfully been characterized both, experimentally (elemental analysis, mass spectrometry, NMR, IR spectroscopy, cyclic voltammetry, XRD, and photophysical properties in solid state and solution) and theoretically (B3LYP/LANL2DZ (Ir)/6-31G(d,p) (ligand's atoms) level of theory) (see Experimental Section, Figures S2–S10 and Tables S2–S10, Supporting Information, for further details).
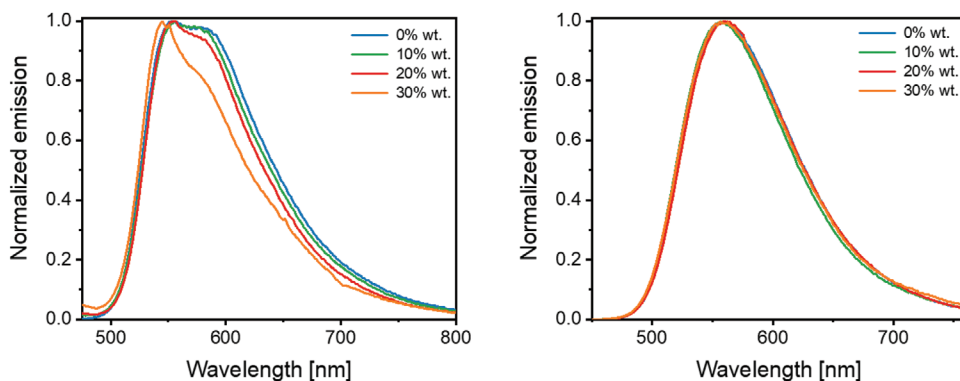
**ADVANCED
SCIENCE NEWS**
www.advancedsciencenews.com

**ADVANCED
FUNCTIONAL
MATERIALS**
www.afm-journal.de

Figure 2. Normalized photoluminescent emission spectra of fresh **A** (left) and **B** (right) films blending different amount of CA (see legend).

2.2. Notes About Morphology and Photoluminescence of Fresh and Stressed CA-based Films

A-based films feature a homogeneous morphology with nanometric roughness in 100 μm^2 sample area (Figure S11, Supporting Information). In line with the semi-crystalline nature of CA, the Young's Modulus slightly increases from ≈0.6 GPa to 3, 3.5, and 5 GPa for 0, 10, 20, and 30 wt.% of CA, respectively. The compatibility between **B** and CA was nicely confirmed by AFM. Both pristine and CA-based films featured a pin-hole-free and homogenous morphology with sub-nanometric roughness (Figure S11, Supporting Information). Unfortunately, viscoelastic mapping measurement of **B**-based thin films was not possible due to attractive electrostatic forces.

As far as the photoluminescence features are concerned, the use of CA-electrolytes strongly impacts them in **A**-films (**Figure 2**). Specifically, CA-free **A**-films exhibit a structured emission band centered at 552 and 582 nm attributed to the pure electronic (π–π/ n-π) transition peak (00) and the first vibronic peak (01), respectively.[32] The photoluminescence quantum yield (PLQY) and excited-state lifetime (τ) values are 13% and 1.15 ns. Blending with CA in small amounts (i.e., 10 and 20 wt.%) does not affect the emission band shape, while the PLQY/τ values are slightly enhanced (Table S11, Supporting Information). Upon addition of 30 wt.% of CA, the emission band is remarkably blue-shifted (545 nm) and the vibrational structure is decreased (I_{01}/I_{00} of 0.78; >0.9 for 0/10/20 wt.% CA). Overall, this results in slightly enhanced radiative rate constants (k_{rad}) from 1.14×10^8 s^{-1} to 1.48×10^8 s^{-1} for 0 and 30 wt.% of CA (Table S11, Supporting Information), respectively. These findings strongly contrast with **B**-films. Here, all of them exhibit a featureless and broad emission band centered at 565 nm that is attributed, according to theoretical calculations, to an admixture of metal-to-ligand and ligand-to-ligand charge transfer excitations [^{3}MLCT(Ir→N^N)/^{3}LLCT(C^N→N^N)], with a remarkable MLCT character (Figure 2). See also photophysical characterization of **B** in Supporting Information.[33]

This is associated to PLQYs of 20/25/25/27% and τ values of 525/606/640/644 ns for 0/10/20/30 wt.% CA, respectively. Thus, k_{rad} does not change upon increasing the amount of CA (e.g., 4.27×10^5/ 4.19×10^5 s^{-1} for 0/30 wt.% CA) (Table S12, Supporting Information).

To shed light onto self-stability of the spin-coated films, morphological/photophysical changes were monitored either over 1 month storage under ambient conditions and dark or after heating them at 50 °C for 1 h. These test conditions were selected to mimic active layer stability of devices.[34,35]

Concerning the morphological changes, the analysis of the relative variation of roughness with respect to that of fresh films indicates that the use of the bio-electrolyte efficiently prevents the tendency to form crystalline and/or aggregated domains regardless of the type of emitter and the stress scenario (**Figure 3** and Figure S11, Supporting Information). In **A**-films, the limit is, however, met with the use of 30 wt.% CA, inferring a maximum of miscibility between **A** and the CA-based electrolyte.

The morphological changes are also reflected in the photoluminescent features. In short, **A**-films show a loss of 70% and *ca.* 50% of the initial PLQY under ambient storage for CA-free and CA-based films, respectively (Figure 3 and Table S11, Supporting Information). This is not associated with remarkable changes in the emission band shape (Figure S12, Supporting Information), while the τ values are equally reduced, confirming short-range rearrangements in the films.[36] Thus, the increase of the non-radiative rate constant (k_{nrad}) is strongly reduced upon using CA electrolytes (*ca.* 30% versus 60% for CA-free films; Figure 3). Likewise, upon thermal stress, CA-based **A**-films show poorly affected k_{rad} and k_{nrad} values for 10% and 20 wt.% CA-films, while they significantly worsen for 30 wt.% CA-films.

In stored and heated **B**-based films, a similar structureless emission band centered at 565 nm is noted compared to fresh films (Figure S13, Supporting Information). In contrast to **A**-films, the changes of PLQY and τ values are very moderate (≈15%) for both stress scenarios (Table S12, Supporting Information), leading to a small impact on the k_{rad} and k_{nrad} values – Figure 3. However, CA-based films showed an enhanced self-stability upon storage with less than 10% change for both k_{rad} and k_{nrad} values, while films with 30 wt.% CA started to exhibit a worse behavior than the reference devices upon thermal stress.

In view of the above finding, we can conclude that **A**-/**B**-based films with 10–20 wt.% CA feature an enhanced self-stability with the respect to the morphological/photophysical features upon storage and thermal stress, while the use of
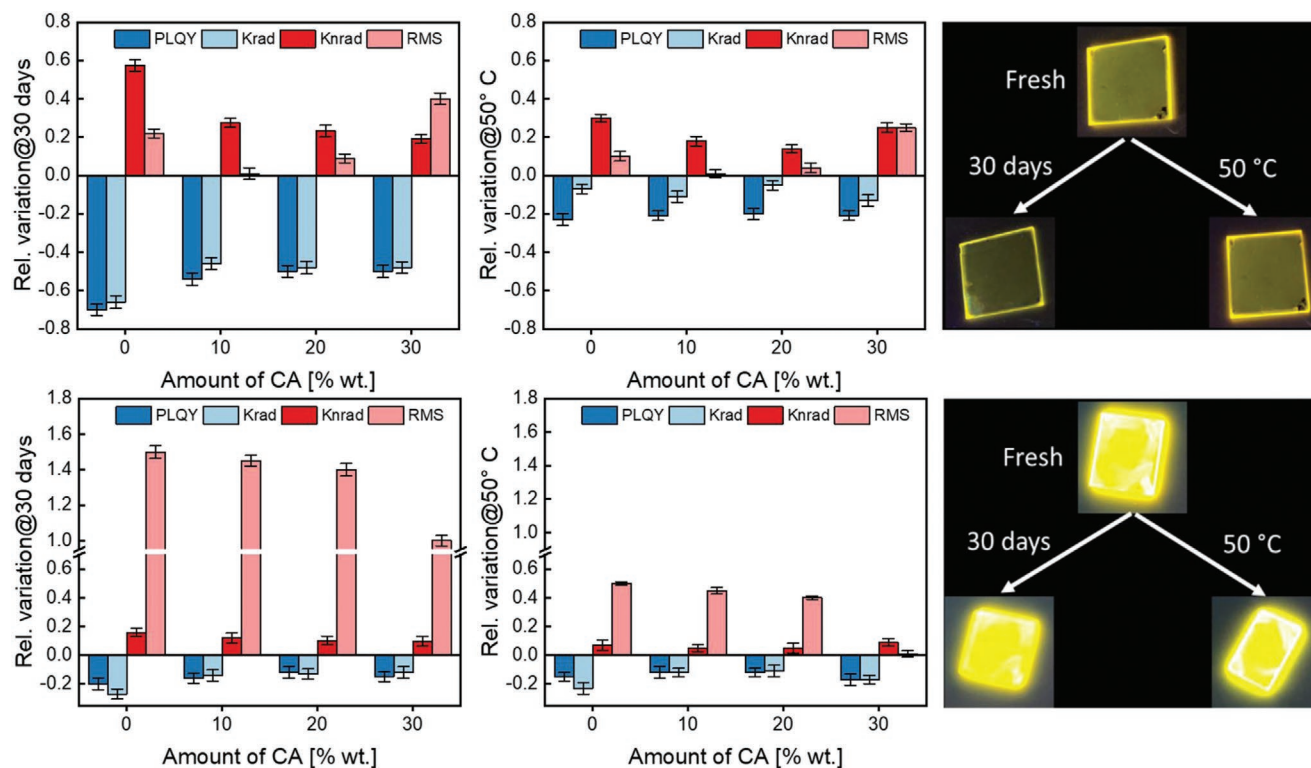
Figure 3. Relative variation upon 30 days of storage in ambient/dark conditions (left) and after 1 h at 50 °C (middle) of PLQY, k_{rad}, k_{nrad}, and roughness of **A** (top) and **B** (bottom) films versus the amount of CA. Right: pictures under UV illumination (305 nm) of **A** (top) and **B** (bottom) films with 30 wt.% of CA before and after self-stability tests.

higher amounts (30 wt.%) in **A**-films is detrimental with respect to resistance at thermal stress. The presence of CA chains separate effectively **A**-/**B**-domains acting as a mechanical spacer. Thus, the processes of aggregation/crystallization are slowed down, resulting in an improved self-stability. In particular, thermal stress is crucial as the working temperature of LECs has recently been reported to span from 40 to 70°C depending on the type of emitter and driving modes.[34,35]

2.3. Notes About Ionic Conductivity in CA-based Films

LECs were fabricated with a double-layered architecture ITO/ PEDOT:PSS(70 nm)/active layer(80–100 nm)/Al(90 nm), in which PEDOT:PSS is poly(3,4-ethylenedioxythiophene) polystyrene sulfonate (see Experimental Section). We studied the device mechanism with respect to ion and electrical conductivities carrying out static electrochemical impedance spectroscopy (EIS) assays at bias ranging from 0 to 4 V with a frequencies scan of 10^0–10^6 Hz.[37,38] The EIS data were analyzed by using a single resistor/capacitor equivalent circuit model that relates to the two dominant dynamic processes upon increasing the applied voltage (Figure S14, Supporting Information). In general, **A**-/**B**-devices show similar Nyquist plots (Figure S14, Supporting Information) consisting of one semicircle from which the resistance (R_{lec}) is ascribed to the dynamics of either EDL's formation at the electrode interface at applied voltages below the energy bandgap of the emitter

($V_{inj} < E_{gap}$) or the reduction of the nondoped region upon charge injection ($V_{inj} > E_{gap}$).

The addition of the CA leads to lower R_{lec} at 0 V and a quick reduction of the R_{lec} in the first regime, indicating that the EDL formation is nicely promoted by the bio-electrolyte. This is also confirmed in the Bode plots (**Figure 4**). At 0 V, the increasing amount of CA reduces the overall resistance in the low-frequency region, while they exhibit similar values at higher frequencies. Furthermore, the presence of CA in the blend leads to a higher corner frequency, which reveals a reduced timescale for ion redistribution.[39] The highest corner frequency is reached with 20 wt.% CA, i.e., 4 Hz/180 Hz compared to 0.1 Hz (estimated)/35 Hz featured by CA-free **A**-/**B**-devices, respectively. This suggests the presence of an optimal composition that maximizes ion motion and, in turn, the formation of EDLs compared to the reference devices.

Another way to analyze the impact of the electrolyte on the device mechanism is the use of the dielectric constant (ε_r) to study the polarization response of the ionic species upon externally applied bias to form EDLs and the ion conductivity (σ) to study the growth of the doped regions. These are calculated at 0 V,[37,38,40] assuming that sandwiched LECs are capacitors embedding polarizable species. CA-free **A**/**B** reference LECs feature σ of 0.55/22.5 nS m^{-1} and ε_r of 6.46/4.32. In general, σ and ε_r are enhanced by increasing the amount of CA, while a major impact in ε_r is noted reaching a threefold increase in 30 wt.% CA devices for both emitters (**Figure 5** and Table S13, Supporting Information). Hence, the use of the bio-electrolyte
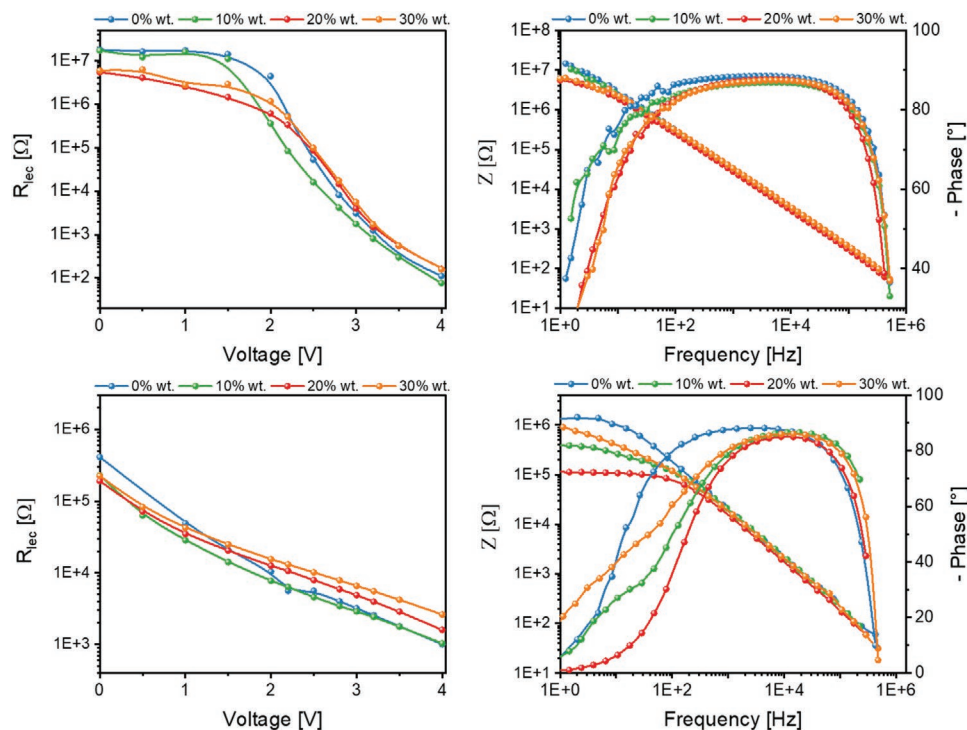
Figure 4. Changes in R_{lec} upon applying different voltages (left) and Bode phase plot (right) for **A**-based (top)/**B**-based (bottom) LECs comprising different %wt. of CA (see legend).

nicely promotes the formation of EDLs and, in turn, the charge injection process is heavily enhanced upon the addition of CA amounts >20 wt.%, as it acts as an efficient ion solvating agent, enhancing ion motion.

Finally, we can analyze the second regime, in which higher R_{lec} values than the reference devices are noted for 20 and 30 wt.% CA devices regardless of the type of emitters. This is desired to prevent the collapse of the p-*i*-n junction by controlling the growing of the doped regions, typically leading to higher stabilities and efficiencies (vide infra).
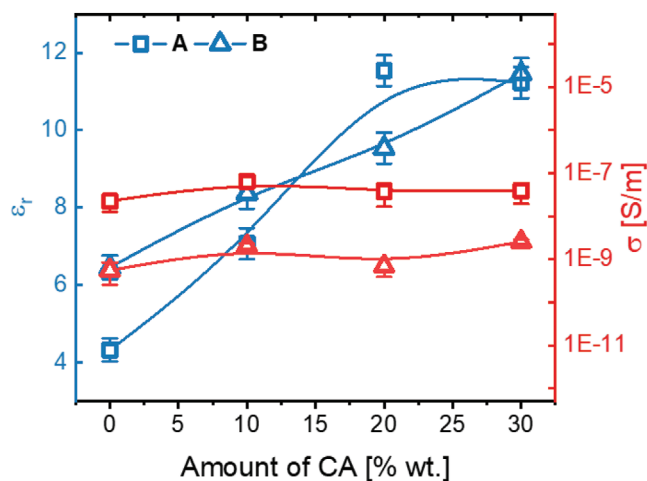

Figure 5. ε_r (blue) and σ (red) of **A**-/**B**-LECs versus the amount of CA in the active layer composition.

2.4. Note about Electroluminescent Response of CA-based LECs

Immediately after their fabrication, LECs were analyzed using pulsed current scheme (5 mA) with a block-wave form at 1000 Hz and duty cycle of 50%,[41] while luminance, x/y Commission Internationale de l'Éclairage 1931 (CIE) coordinates, electrical behavior, and working temperature were monitored over time (**Figure 6** and **Table 1**; Figure S15, Supporting Information).

As expected by the EIS assays, all the **A**/**B**-devices show the typical LEC behavior, in which the initial average voltage is reduced reaching a steady-state voltage regime of *ca.* 3 V, while the luminance raises up. In **A**-based devices, maximum luminances of 3580/3780/3750/3400 cd m^{-2} and efficiencies of 14.3/15.1/15.0/13.6 cd A^{-1} were noted for 0/10/20/30 wt.% CA, respectively. The emission spectra hold constant during the device lifespan, showing a similar yellow emission centered at 553 nm. The electroluminescence spectra are associated with x/y CIE color coordinates shifting from 0.43/0.54 (0 wt.% CA) to 0.47/0.52 (30 wt.% CA), with color purity >0.95 in all the cases. Here, the E_{0-0} band (2.5 eV) holds regardless of the amount of CA, while the full width at half maximum is 80/85/85/93 nm for 0/10/20/30 wt.% CA. Thus, the same emissive excited state is involved (i.e., same E_{0-0} band), but the CA may promote conformational changes leading to different vibrational distribution.[10] Likewise, **B**-LECs show an increase in the luminous intensity when the applied voltage reduces, reaching maximum values of 330/300/600/550 cd m^{-2} that correspond to efficacies of 1.3/1.2/2.4/2.2 cd A^{-1} for devices embedding 0/10/20/30 wt.% CA, respectively. This is followed
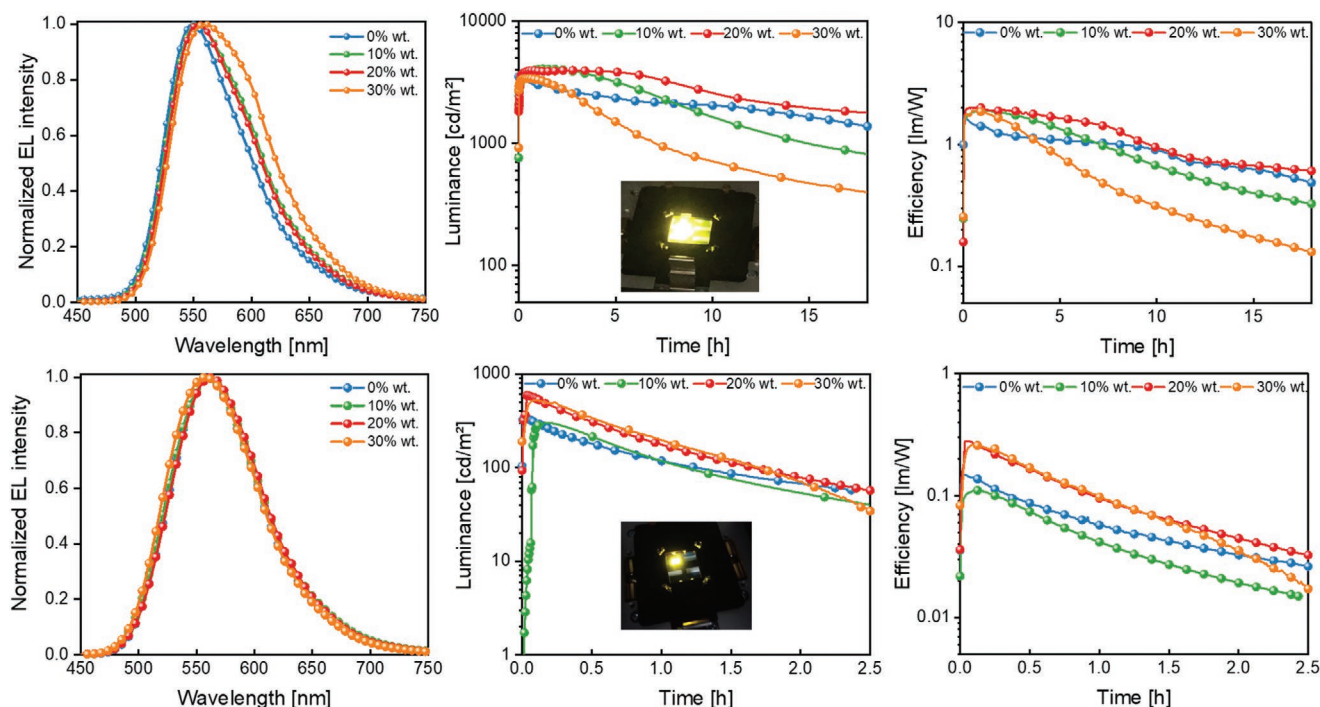
Figure 6. Normalized initial electroluminescence spectra (left), temporal changes of luminance (middle), and efficiency (right) of **A** (top) and **B** (bottom) LECs with different CA amounts (see legend) driven at pulsed current of 5 mA. Insets: pictures of pixel in operando.

by a quick decrease of the luminance, achieving lifetimes of 0.6/0.7/0.5/0.65 h. In all cases, the electroluminescent band is featureless and centered at 562 nm, corresponding to x/y CIE color coordinates of 0.43/0.54. This matches a *quasi*-spectral yellow emission, with a color purity of 0.94, stable over the entire device lifespan.

A direct comparison of device stability and efficiencies operating at different luminance intensities and average voltage profiles is not straightforward.[42] Thus, Figure 6 displays the changes in the device efficiency (lm W^{-1}) over time that take into account the different voltage profiles. Noteworthy, devices embedding 20 wt.% CA are the most efficient along the entire device lifespan compared to the reference devices of both emitters. With regards to the stability, two approaches were considered: i) extrapolated lifetime at defined luminance[43,44] and ii) total emitted energy (E_{tot}).[39,45–47] With the former, the extrapolated lifetime (T_2) at defined luminance (L_2) is calculated

applying the following equation: $T_2 = T_1 \left(\dfrac{L_1}{L_2} \right)^{A_F}$, in which T_1 and L_1 are the experimentally measured lifetime and maximum luminance, and A_F is an exponential factor to be 1.5.[48–50] E_{tot} is calculated by integrating the radiant flux curve until the time needed to reach one-fifth of the maximum luminance as an upper limit definition.[45] **Figure 7** displays how both parameters are enhanced with respect to the reference devices. In line with the self-stability and EIS measurements, the use of 20 wt.% CA-based electrolytes led to the highest values of stability, namely T_2 of 3000/ 7.4 h and E_{tot} of 153/ 0.7 J values for **A**-/**B**-based LECs, respectively. Compared to CA-free devices, those values represent ≈2-/ 2- (T_2) and 4-/ 2- (E_{tot}) fold enhancement. Higher amounts of CA in **B**-devices did not significantly affect the device performance, while it is detrimental for A-devices. This must be ascribed to the working temperature that reaches up to 45 and 55 °C for **A**- and **B**-devices, respectively. Indeed, the

Table 1. Figures-of-merit of **A**-/**B**-LECs driven at 5 mA, 1 kHz, and 50% duty cycle.

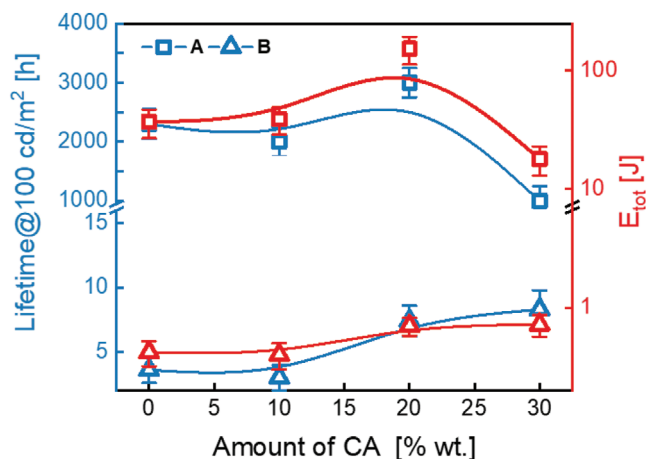| Emitter	CA [%wt.]	Initial voltage [V]	Luminance [cd m^{-2}]	λ_{EL} [nm]	Efficacy [cd A^{-1}]	Lifetime [h]	Efficiency [lm W^{-1}]	Lifetime@100 cd m^{-2} [h]	E_{tot} [J]
A	0	4.02	3580	550	14.3	11	1.7	2300	37
	10	3.50	3780	553	15.1	8.5	1.9	2000	39
	20	3.10	3750	553	15.0	12.5	2.0	3000	153
	30	3.45	3400	559	13.6	4.5	1.9	1000	18
B	0	4.55	330	562	1.3	0.6	0.15	3.6	0.42
	10	3.90	300	562	1.2	0.7	0.11	3.0	0.38
	20	4.00	600	562	2.4	0.5	0.28	7.4	0.70
	30	3.60	550	562	2.2	0.65	0.25	8.3	0.72

Figure 7. Relative lifetime@100 cd m^{-2} (blue) and total emitted energy (red) of **A**-/**B**-LECs versus different CA amounts in the active layer.

self-stability under thermal stress of 30 wt.% CA in **A**-films (Figure 3) shows a significant change in the film morphology and reduction of the PLQY after 1 h at 50 °C. In contrast, **B**-films show excellent thermal self-stability regardless of the amount of CA.

All-in-all, the improvement in the device stability goes hand-in-hand with that of the efficiency, concluding that 20 wt.% CA bio-electrolytes clearly outperform the respective reference devices overcoming the common trade-off leading to performance loss noted in the prior art.[13–16]

3. Conclusion

This work sets in the first family of fully biogenic electrolytes applied to LECs, overcoming the loss performance noted when green electrolytes have been applied,[13–16] and outperforming both, traditional reference devices and the prior art in LECs with biodegradable polymer and DNA-hybrid electrolytes. This might represent a significant step forward towards meeting the green (opto)electronic requirements for the future market entrance of the LEC technology. In detail, we have shown that this biogenic cellulose-based electrolyte provides enhanced device self-stability (reduced impact on the morphology and photophysical features upon storage and thermal stress) and device performance (4-/2-fold enhanced efficacy and stability) using different types of emitters, such as iTMCs and CPs. This holds true for electrolytes with up to 30 wt.% CA, as changes in the film morphology and photophysical features are noted in the self-stability tests for CP-films.. Here, chemical modification to increase the hydrophobic character of CA is envisaged to circumvent this issue. This is an on-going research line in our laboratories as the chemical routes to modify CA are well-known and easily accessible, leading to plenty of room to further enhance the LEC performance. Indeed, this work shows a fresh approach that strongly reinforces the relevance of carbohydrate-based electrolytes not only for batteries, supercapacitors, and photovoltaics,[24,25] but also for lighting purposes beyond its traditional use as substrates.[26]

4. Experimental Section

Materials: All the reagents and materials were obtained from commercial sources and used without further purification. CA has been obtained from coniferous pulp. All the reactions carried out for the synthesis of the complex [Ir(dfppy)$_2$(dbbpy)]PF$_6$ (**B**) were performed under Ar atmosphere and anhydrous conditions. The precursors ([Ir(dfppy)$_2$(μ-Cl)]$_2$; [Ir(dfppy)$_2$(NCMe)$_2$]PF$_6$; dfppy = 2-(2,4)-difluorophenyl-pyridinyl)[51] and the diimine ligand N,N'-dibutyl-2,2'-bipyridine-4,4'-dicarboxamide (dbbpy)[52] were synthetized following reported methods. Complex **B** has been synthesized following the reaction reported in Figure S2 (Supporting Information): a solution of 0.21 g (0.26 mmol) of [Ir(dfppy)$_2$(CH$_3$CN)$_2$]PF$_6$ in a mixture of methanol and dichloromethane (1:2, v/v) was treated with 0.09 g (0.26 mmol) of dbbpy. The resulted yellow mixture was stirred for 6 h at room temperature and the solution evaporated to dryness. The solid residue obtained was treated with diethyl ether, yielding complex **B** as a yellow solid (0.21 g, 75%). Anal. Calc. for C$_{42}$H$_{38}$F$_{10}$IrN$_6$O$_2$P: C, 47.06; H, 3.57; N, 7.84. Best analyses found: C, 43.93; H, 3.37; N, 7.85 (Elemental analyses fit well for B·1.5CH$_2$Cl$_2$. C$_{43.5}$H$_{41}$Cl$_3$F$_{10}$IrN$_6$O$_2$P: C, 43.56; H, 3.45; N, 7.01). ESI(+): $^m/_z$ 927 [M]$^+$ (100%). IR (cm^{-1}): ν(N-H) 3463(m); ν(C-H) 3127 (w), 3072 (w), 2959 (m), 2926 (m), 2871 (w), 2852 (w); ν(C = O) 1674 (s); ν(C-H ring) 1600 (s), 1575 (s), 1540 (s), 1478 (s), 1432 (m), 1406 (s); ν(C-F) 1297 (m); ν(P-F) 835 (vs). ^{1}H NMR (400 MHz, CDCl$_3$, δ): 8.78 (s, 2H, H$^{3'}$$_{bpy}$); 8.33 (d, J$_{H-H}$ = 8.8 Hz, 2H, H^2$_{dfppy}$); 8.05 (d, J$_{H-H}$ = 5.7 Hz, 2H), 7.97 (d, J$_{H-H}$ = 5.7 Hz, 2H) (H$^{5'}$$_{bpy}$ and H$^{6'}$$_{bpy}$); 7.85 (t, J$_{H-H}$ = 7.9 Hz, 2H, H^3$_{dfppy}$); 7.43 (d broad, J$_{H-H}$ = 5.6 Hz, 4H, NH and H^5$_{dfppy}$); 7.07 (t, J$_{H-H}$ = 6.8 Hz, 2H, H^4$_{dfppy}$); 6.61 (pst, ^{3}J$_{F-H}$ = 11.5 Hz, 2H, H^7$_{dfppy}$); 5.68 (dd, ^{3}J$_{F-H}$ = 8.3 Hz, J$_{H-H}$ = 2.2 Hz, 2H, H^9$_{dfppy}$); 3.50 (quad, J$_{H-H}$ = 6.9 Hz, 4H, CH$_2$CH$_2$CH$_2$CH$_3$); 1.68 (quint, J$_{H-H}$ = 7.6 Hz, 4H, CH$_2$-CH$_2$-CH$_2$-CH$_3$); 1.42 (sx, J$_{H-H}$ = 7.6 Hz, 4H, CH$_2$CH$_2$CH$_2$CH$_3$); 0.95 (t, J$_{H-H}$ = 7.2 Hz, 6H, CH$_2$CH$_2$CH$_2$CH$_3$). ^{13}C{^{1}H} NMR (100.6 MHz, CDCl$_3$, δ): 164.3 (d, ^{3}J$_{F-C}$ ≈ 8 Hz, C^{12}$_{dfppy}$); 164.1 (d, ^{1}J$_{F-C}$ ≈ 230 Hz, C^6$_{dfppy}$ or C^8$_{dfppy}$); 163.8 (s, CO), 155.7 (s, C$^{2'}$$_{bpy}$ or C$^{4'}$$_{bpy}$); 152.9 (d, J$_{F-C}$ = 6 Hz, C^{10}$_{dfppy}$ or C^{11}$_{dfppy}$); 150.88 (s, C$^{6'}$$_{bpy}$ or C$^{5'}$$_{bpy}$); 148.5 (s, C^5$_{dfppy}$); 146.7 (s, C$^{2'}$$_{bpy}$ or C$^{4'}$$_{bpy}$); 139.7 (s, C^3$_{dfppy}$); 128.2 (s, C$^{6'}$$_{bpy}$ or C$^{5'}$$_{bpy}$); 127.6 (d, J$_{F-C}$ ≈ 250 Hz, C^6$_{dfppy}$ or C^8$_{dfppy}$); 127.4 (d, J$_{F-C}$ ≈ 6 Hz, C^{10}$_{dfppy}$ or C^{11}$_{dfppy}$); 124.3 (s, C^2$_{dfppy}$); 124.0 (s, C^4$_{dfppy}$); 122.4 (s, C$^{3'}$$_{bpy}$); 114.1 (d, ^{2}J$_{F-C}$ ≈ 20 Hz, C^9$_{dfppy}$); 99.7 (d, ^{2}J$_{F-C}$ ≈ 26 Hz, C^7$_{dfppy}$); 40.8 (s, CH$_2$CH$_2$CH$_2$CH$_3$); 31.2 (s, CH$_2$CH$_2$CH$_2$CH$_3$); 20.3 (s, CH$_2$CH$_2$CH$_2$CH$_3$); 13.8 (s, CH$_2$CH$_2$CH$_2$CH$_3$). ^{19}F NMR (376.5 MHz, CDCl$_3$, δ): -70.4 (d, J$_{F-F}$ = 716 Hz); -104.5 (d, J$_{F-F}$ = 11.2 Hz, 2F, F^6); -107.8 (d, J$_{F-F}$ = 11.2 Hz, 2F, F^8). ^{31}P{^{1}H} NMR (162.1 MHz, CDCl$_3$, δ): -144.2 (sp, J$_{P-F}$ = 716, PF$_6$).

IR spectra were recorded on a PerkinElmer Spectrum UATR Two FT-IR Spectrometer with the diamond crystal ATR option, in the range between 4000 and 450 cm^{-1}. Elemental analysis was carried out in a Perkin-Elmer 2400 CHNS/O microanalyzer. Mass spectra were recorded on a Microflex MALDI-TOF Bruker spectrometer. NMR spectra were recorded on a Bruker ARX400 spectrometer. Chemical shifts are reported in parts per million (ppm) relative to external standards (SiMe$_4$ for ^{1}H and ^{13}C{^{1}H} and CFCl$_3$ for ^{19}F{^{1}H}) and coupling constants in Hz. ^{1}H and ^{13}C{^{1}H} NMR spectra were assigned following the numbering scheme shown in Figure S2 (Supporting Information), by means of 2D experiments (^{1}H-^{1}H COSY and ^{1}H-^{13}C HSQC and HMBC). X-ray intensity data were collected with a Bruker D8 QUEST (PHOTON 100 CMOS) area-detector diffractometer, using graphite-monochromatic Mo-K$_\alpha$ radiation. The images were collected and processed using Bruker APEX3 and SAINT programs, carrying out the absorption correction at this point by semi-empirical methods using SADABS. The structures were solved by intrinsic phasing using SHELXT,[53] and refined by full-matrix least squares on F^2 with SHELXL, using the WINGX program suite.[54,55] UV–vis spectra in solution were recorded on an Agilent 8453 spectrophotometer. The excitation and emission spectra in solution as well as excited state lifetime measurements were obtained on an Edinburgh FLS 1000 Fluorescence spectrometer. For the measurements, it was employed a Picosecond Pulsed Diode LED with a wavelength of 375 nm. PLQYs were measured using an N-M101 integrating sphere on an Edinburgh FLS 1000 Fluorescence spectrometer.

Cyclic voltammetry measurements were carried out on a Voltalab PST050 electrochemical workstation, using a solution of tetra-butylammonium hexafluorophosphate (NBu$_4$PF$_6$) as the supporting electrolyte. A conventional three-electrode configuration was used, consisting of a platinum spar working electrode, a platinum wire counter electrode, and an Ag/AgCl reference electrode.

Thin Film Preparation: Master solutions for each component were separately prepared. Blend solution were prepared by mixing the master solutions together in a desired mass ratio, followed by stirring on a magnetic hot plate for 1h. **A** was dissolved in tetrahydrofuran (THF) at a concentration of 7 mg mL^{-1} and stirred for 7 h, **B** was dissolved in acetonitrile (ACN) at concentration of 15 mg mL^{-1} while CA and THABF$_4$ were dissolved at concentration of 5 and 20 mg mL^{-1}, respectively either in THF or ACN.

For self-stability tests, cleaned quartz substrates were used and they were stored in ambient conditions. Thin films were prepared from a filtered solution of the desired blend by spin-coating it at 800 rpm for 30 s, at 1500 rpm for 30 s, and at 3000 rpm for an additional 10 s.

AFM measurements were acquired using an MFP-3D Origin+ (Asylum Research), and further elaborate with Gwyddion evaluation software. The nano-mechanical properties were measured using AMFM mode for the acquisition of modulus in high frequency (≈1.6 MHz). The cantilever spring constants used in this work were around 20–30 N m^{-1}. The tip radius was calibrated with internal reference.

The photoluminescence spectra and PLQY values in thin film were measured with an FS5 Spectrofluorometer with integrating sphere SC-30 (Edinburgh Instruments). The excited-state lifetimes were acquired with a TCSPC diode at λ 377.6 nm or 454 nm and their average value can be obtained using the following equation:[56]

$$\tau = \frac{A_1\tau_1^2 + A_2\tau_2^2}{A_1\tau_1 + A_1\tau_1} \tag{2}$$

Theoretical Calculations: Calculations for **B** (acetonitrile solution) were carried out with the Gaussian 09 package,[57] using Becke's three-parameter functional combined with Lee-Yang-Parr's correlation functional (B3LYP) in the singlet state (S$_0$), and the unrestricted U-B3LYP in the triplet state (T$_1$).[58,59] According to previous theoretical calculations for iridium complexes, the optimized ground state geometry were calculated at the B3LYP/LANL2DZ (Ir)/6-31G(d,p) (ligands' atoms) level. The S$_0$ geometry was found to be a true minimum as no negative frequencies in the vibrational frequency study of the final geometry were found. Density functional theory (DFT) and time-dependent-DFT (TD-DFT)-DFT calculations were carried out using the polarized continuum model approach,[60] implemented in the Gaussian 09 software. The MO diagrams and the orbital contributions were generated with Gaussian 09 software and Gauss-Sum program,[61] respectively. The emission energy was calculated as the difference of the optimized T$_1$ geometry for both states.

Device Fabrication and Characterization: ITO substrates were purchased from Naranjo Substrates with an ITO thickness of 130 nm. They were extensively cleaned using detergent, water, ethanol, and propan-2-ol as solvents in an ultrasonic bath (frequency 37–70 Hz) for 15 min each. Afterward, the slides were dried with inert gas and put in a UV–ozone cleaner for 8 min. The clean plates were coated with 70 nm PEDOT:PSS layers via spin coating to increase the device reproducibility. To this end, an aqueous solution of PEDOT:PSS was filtered and mixed with propan-2-ol in a ratio of 3:1. From this solution, 50 µL were dropped onto the substrate at a rotation speed of 2000 rpm and spun for 60 s. The resulting layers were dried on a hotplate at 120 °C and stored under N$_2$. The active layers were deposited from blend solutions and spin coated at 800 rpm for 30 s, at 1500 rpm for 30 s, and at 3000 rpm for an additional 10 s, resulting in 80–100 nm thick film. For functional LEC fabrication, glass/ITO/PEDOT:PSS substrates were used and after the deposition of the active layer the devices were dried under vacuum for 2 h and transferred to an inert atmosphere glovebox. Finally, aluminum cathode (90 nm) was thermally evaporated onto the active layer using a shadow mask under high vacuum (<10^{-6} mbar) in an Angstrom Covap evaporator integrated into the inert atmosphere glovebox. Time

dependence of luminance, voltage, and current was measured by applying constant and/or pulsed voltage and current by monitoring the desired parameters simultaneously by using Avantes spectrophotometer (Avaspec-ULS2048L-USB2) in conjunction with a calibrated integrated sphere Avasphere 30-Irrad and Botest OLT OLED Lifetime-Test System. Electroluminescence spectra were recorded using the above-mentioned spectrophotometer. Electrochemical impedance spectroscopic assays (EIS) were carried out with a potentiostat/galvanostatic (Metrohm µAutolabIII) equipped with a frequency response analyzer module (FRA2). Measurements were performed at the applied voltage range from 0 to 4 V and fitted with the Nova 2.1 software using the circuit model shown in Figure S14 (Supporting Information). R_{LEC} represents the effective resistance of the active layer, including injection resistances, CPE_{LEC} represents the capacitance of the two electrodes contacting the film. The second resistor (R_{series}) represents all external resistances, including those of the ITO and Al electrodes, and L_{cables} represents the inductance of the measurement cables. The AC signal amplitude was set to 10 mV, modulated in a frequency range from 10^0 to 10^6 MHz.

Statistical Analysis: Thin films statistic involve three replicates for each composition, while the device statistics involve up to five different devices, i.e., a total number of 20 pixels. The absence of outliers had been confirmed via t-test. The data reported in the text and in the tables refer to the average values. Relative standard deviation span from 1% to 10%. The software OriginPro 2020 has been used for data analysis and evaluation.

Supporting Information

Supporting Information is available from the Wiley Online Library or from the author.

Conflict of Interest

The authors declare no conflict of interest.

Data Availability Statement

The data that support the findings of this study are available from the corresponding author upon reasonable request.

[1] E. Fresta, R. D. Costa, *J. Mater. Chem. C* **2017**, *5*, 5643.

[2] A. Asadpoordarvish, A. Sandström, C. Larsen, R. Bollström, M. Toivakka, R. Österbacka, L. Edman, *Adv. Funct. Mater.* **2015**, *25*, 3238.

[3] S. van Reenen, M. Kemerink, in *Light. Electrochem. Cells*, Springer International Publishing, Cham, **2017**, pp. 3.

[4] J. Mindemark, S. Tang, H. Li, L. Edman, *Adv. Funct. Mater.* **2018**, *28*, 1801295.

[5] I. Gerz, E. M. Lindh, P. Thordarson, L. Edman, J. Kullgren, J. Mindemark, *ACS Appl. Mater. Interfaces* **2019**, *11*, 40372.

[6] A. Sandström, L. Edman, *Energy Technol.* **2015**, *3*, 329.

[7] R. D. Costa, *Light-Emitting Electrochemical Cells*, Springer International Publishing, Cham, **2017**.

[8] E. Fresta, G. U. Mahoro, L. M. Cavinato, J.-F. J. Lohier, J.-L. J. Renaud, S. Gaillard, R. D. Costa, *Adv. Opt. Mater.* **2021**, 2101999.

[9] E. Fresta, A. Charisiadis, L. M. Cavinato, N. Palandjian, K. Karikis, V. Nikolaou, G. Charalambidis, A. G. Coutsolelos, R. D. Costa, *Adv. Photonics Res.* **2021**, *2*, 2000188.

[10] E. Fresta, J. Dosso, J. Cabanillas-González, D. Bonifazi, R. D. Costa, *Adv. Funct. Mater.* **2020**, *30*, 1906830.

[11] S. Kanagaraj, A. Puthanveedu, Y. Choe, *Adv. Funct. Mater.* **2020**, *30*, 1907126.

[12] J. R. Adsetts, Z. Whitworth, K. Chu, L. Yang, C. Zhang, Z. Ding, *Chem Electro Chem* **2022**, https://doi.org/10.1002/celc.202101512.

[13] J. Zimmermann, N. Jürgensen, A. J. Morfa, B. Wang, S. Tekoglu, G. Hernandez-Sosa, *ACS Sustainable Chem. Eng.* **2016**, *4*, 7050.

[14] N. Jürgensen, J. Zimmermann, A. J. Morfa, G. Hernandez-Sosa, *Sci. Rep.* **2016**, *6*, 36643.

[15] J. Zimmermann, L. Porcarelli, T. Rödlmeier, A. Sanchez-Sanchez, D. Mecerreyes, G. Hernandez-Sosa, *Adv. Funct. Mater.* **2018**, *28*, 1705795.

[16] S. Tekoglu, M. Held, M. Bender, G. N. Yeo, A. Kretzschmar, M. Hamburger, J. Freudenberg, S. Beck, U. H. F. Bunz, G. Hernandez-Sosa, *Adv. Sustain. Syst.* **2021**, *5*, 2000203.

[17] a) S. Tang, L. Edman, *J. Phys. Chem. Lett.* **2010**, *1*, 2727; b) E. Auroux, A. Sandström, C. Larsen, E. Zäll, P. Lundberg, T. Wågberg, L. Edman, *Adv. Electron. Mater.* **2021**, *7*, 2100253.

[18] E. Fresta, M. A. Monclús, M. Bertz, C. Ezquerro, J. M. Molina-Aldareguia, J. R. Berenguer, M. Kunimoto, T. Homma, R. D. Costa, *Adv. Opt. Mater.* **2020**, *8*, 2000295.

[19] H. M. Park, M. Misra, L. T. Drzal, A. K. Mohanty, *Biomacromolecules* **2004**, *5*, 2281.

[20] A. K. Mohanty, A. Wibowo, M. Misra, L. T. Drzal, *Polym. Eng. Sci.* **2003**, *43*, 1151.

[21] N. I. Harun, R. M. Ali, A. M. M. Ali, M. Z. A. Yahya, *Ionics (Kiel)* **2012**, *18*, 599.

[22] E. Auroux, A. Sandström, C. Larsen, E. Zäll, P. Lundberg, T. Wågberg, L. Edman, *Adv. Electron. Mater.* **2021**, *7*, 2100253.

[23] D. Lee, Y. W. Lim, H. G. Im, S. Jeong, S. Ji, Y. H. Kim, G. M. Choi, J. U. Park, J. Y. Lee, J. Jin, B. S. Bae, *ACS Appl. Mater. Interfaces* **2017**, *9*, 24161.

[24] L. Liu, N. Solin, O. Inganäs, *Adv. Energy Mater.* **2021**, *11*, 2003713.

[25] L. M. Cavinato, E. Fresta, S. Ferrara, R. D. Costa, *Adv. Energy Mater.* **2021**, *11*, 2100520.

[26] M. Reimer, C. Zollfrank, *Adv. Energy Mater.* **2021**, *11*, 2003866.

[27] S. Tang, W.-Y. Tan, X.-H. Zhu, L. Edman, *Chem. Commun.* **2013**, *49*, 4926.

[28] J. Fang, P. Matyba, L. Edman, *Adv. Funct. Mater.* **2009**, *19*, 2671.

[29] J. M. Fernández-Hernández, S. Ladouceur, Y. Shen, A. Iordache, X. Wang, L. Donato, S. Gallagher-Duval, M. de Anda Villa, J. D. Slinker, L. De Cola, E. Zysman-Colman, *J. Mater. Chem. C* **2013**, *1*, 7440.

[30] F. P. Wenzl, P. Pachler, C. Suess, A. Haase, E. J. W. List, P. Poelt, D. Somitsch, P. Knoll, U. Scherf, G. Leising, *Adv. Funct. Mater.* **2004**, *14*, 441.

[31] M. D. Weber, J. E. Wittmann, A. Burger, O. B. Malcıoğlu, J. Segarra-Martí, A. Hirsch, P. B. Coto, M. Bockstedte, R. D. Costa, *Adv. Funct. Mater.* **2016**, *26*, 6737.

[32] E. M. Lindh, P. Lundberg, T. Lanz, J. Mindemark, L. Edman, *Sci. Rep.* **2018**, *8*, 6970.

[33] R. D. Costa, E. Ortí, H. J. Bolink, S. Graber, S. Schaffner, M. Neuburger, C. E. Housecroft, E. C. Constable, *Adv. Funct. Mater.* **2009**, *19*, 3456.

[34] J. Ràfols-Ribé, N. D. Robinson, C. Larsen, S. Tang, M. Top, A. Sandström, L. Edman, *Adv. Funct. Mater.* **2020**, *30*, 1908649.

[35] E. Fresta, J. Dosso, J. Cabanillas-Gonzalez, D. Bonifazi, R. D. Costa, *ACS Appl. Mater. Interfaces* **2020**, *12*, 28426.

[36] D. Ma, T. Tsuboi, Y. Qiu, L. Duan, *Adv. Mater.* **2017**, *29*, 1603253.

[37] S. B. Meier, D. Hartmann, A. Winnacker, W. Sarfert, *J. Appl. Phys.* **2014**, *116*, 104504.

[38] A. Munar, A. Sandström, S. Tang, L. Edman, *Adv. Funct. Mater.* **2012**, *22*, 1511.

[39] A. Mishra, M. Alahbakhshi, R. Haroldson, L. D. Bastatas, Q. Gu, A. A. Zakhidov, J. D. Slinker, *Adv. Opt. Mater.* **2020**, *8*, 2000226.

[40] S. van Reenen, R. A. J. Janssen, M. Kemerink, *Adv. Funct. Mater.* **2012**, *22*, 4547.

[41] S. B. Meier, D. Tordera, A. Pertegás, C. Roldán-Carmona, E. Ortí, H. J. Bolink, *Mater. Today* **2014**, *17*, 217.

[42] K. Youssef, Y. Li, S. O'Keeffe, L. Li, Q. Pei, *Adv. Funct. Mater.* **2020**, *30*, 1909102.

[43] M. H. Bowler, A. Mishra, A. C. Adams, C. L. D. Blangy, J. D. Slinker, *Adv. Funct. Mater.* **2020**, *30*, 1906715.

[44] M. D. Moore, M. H. Bowler, J. E. Reynolds, V. M. Lynch, Y. Shen, J. D. Slinker, J. L. Sessler, *ACS Appl. Mater. Interfaces* **2018**, *10*, 24699.

[45] M. D. Weber, E. Fresta, M. Elie, M. E. Miehlich, J.-L. Renaud, K. Meyer, S. Gaillard, R. D. Costa, *Adv. Funct. Mater.* **2018**, *28*, 1707423.

[46] E. Fresta, M. D. Weber, J. Fernandez-Cestau, R. D. Costa, *Adv. Opt. Mater.* **2019**, *7*, 1900830.

[47] G. Kalyuzhny, M. Buda, J. McNeill, P. Barbara, A. J. Bard, *J. Am. Chem. Soc.* **2003**, *125*, 6272.

[48] K. Lin, J. Xing, L. N. Quan, F. P. G. de Arquer, X. Gong, J. Lu, L. Xie, W. Zhao, D. Zhang, C. Yan, W. Li, X. Liu, Y. Lu, J. Kirman, E. H. Sargent, Q. Xiong, Z. Wei, *Nature* **2018**, *562*, 245.

[49] P. Wellmann, M. Hofmann, O. Zeika, A. Werner, J. Birnstock, R. Meerheim, G. He, K. Walzer, M. Pfeiffer, K. Leo, *J. Soc. Inf. Disp.* **2005**, *13*, 393.

[50] X. Dai, Z. Zhang, Y. Jin, Y. Niu, H. Cao, X. Liang, L. Chen, J. Wang, X. Peng, *Nature* **2014**, *515*, 96.

[51] E. Marchi, M. Locritani, M. Baroncini, G. Bergamini, R. Sinisi, M. Monari, C. Botta, W. Mróz, M. Bandini, P. Ceroni, V. Balzani, *J. Mater. Chem. C* **2014**, *2*, 4461.

[52] C. Sahin, A. Goren, S. Demir, M. S. Cavus, *New J. Chem.* **2018**, *42*, 2979.

[53] G. M. Sheldrick, *Acta Crystallogr. Sect. A Found. Crystallogr.* **2015**, *71*, 3.

[54] G. M. Sheldrick, *Acta Crystallogr. Sect. C Struct. Chem.* **2015**, *71*, 3.

[55] L. J. Farrugia, *J. Appl. Crystallogr.* **1999**, *32*, 837.

[56] R. W. K. Leung, S.-C. A. Yeh, Q. Fang, *Biomed. Opt. Express* **2011**, *2*, 2517.

[57] G. E. S. M. J. Frisch, G. W. Trucks, H. B. Schlegel, B. M. M. A. Robb, J. R. Cheeseman, G. Scalmani, V. Barone, H. P. H. G. A. Petersson, H. Nakatsuji, M. Caricato, X. Li, M. H. A. F. Izmaylov, J. Bloino, G. Zheng, J. L. Sonnenberg, T. N. M. Ehara, K. Toyota, R. Fukuda, J. Hasegawa, M. Ishida, J. Y. Honda, O. Kitao, H. Nakai, T. Vreven, J. A. Montgomery, E. B. J. E. Peralta, F. Ogliaro, M. Bearpark, J. J. Heyd, J. N. K. N. Kudin, *Gaussian 09, Revision B.01.*, Gaussian, Inc., Wallingford, CT **2010**.

[58] C. Lee, W. Yang, R. G. Parr, *Phys. Rev. B* **1988**, *37*, 785.

[59] A. D. Becke, *Phys. Rev. A* **1988**, *38*, 3098.

[60] M. Cossi, N. Rega, G. Scalmani, V. Barone, *J. Chem. Phys.* **2001**, *114*, 5691.

[61] N. M. O'boyle, A. L. Tenderholt, K. M. Langner, *J. Comput. Chem.* **2008**, *29*, 839.